INTERNATIONAL JOURNAL FOR NUMERICAL METHODS IN FLUIDS, VOL. 23, 883–895 (1996)

PERFORMANCE PREDICTION OF A BACKSWEPT CENTRIFUGAL IMPELLER AT OFF-DESIGN POINT CONDITIONS

MOU-JIN ZHANG
Department of Fluid Engineering, Xian Jiaotong University, Xian 710049, People's Republic of China
M. J. POMFRET
Tuen Mun Technical Institute, Hong Kong
AND
C. M. WONG
Department of Mechanical and Marine Engineering, Hong Kong Polytechnic University, Hung Hom, Kowloon, Hong Kong

SUMMARY

The internal flows inside a backswept centrifugal impeller at off-design point conditions are analysed by solving the fully three-dimensional Navier–Stokes equations coupled with the k–ε two- equation turbulence model. Conditions analysed have flow rates of 85 per cent and 113 per cent of the design rate. The calculated results are compared with published experimental data and the comparison shows good agreement. A jet wake structure occurs near the outlet of the impeller for each of the two off-design flow rates and the location and size of the jet wake structure seem to be independent of the flow rate.

KEY WORDS: N-s solver; turbomachinery

INTRODUCTION

Centrifugal compressors for industrial applications need a high efficiency and a wide range of operation to minimize power consumption and to satisfy the variable demands of operation. To meet and improve these requirements necessitates a complete understanding of the internal flow mechanisms. The flows inside centrifugal impellers are very complex because of the rotation, viscous effects and complex geometry, especially for the three-dimensional centrifugal impellers which are widely used nowadays; thus any change in operating conditions will affect the performance of the impeller greatly. It is necessary for designers to know accurately about the performance and the operating range at an early stage of development.

For many years, researchers have been improving predictions of the flows inside centrifugal impellers with numerical studies and progress has advanced steadily. In recent years especially, with the advances in computational fluid dynamics, it is now possible to predict the performance of centrifugal impellers by solving the three-dimensional viscous flow equations instead of inviscid approximations, as has been shown by researchers such as Gasey *et al.*,[1] Denton,[2] Dawes,[3] Hathaway

CCC 0271–2091/96/090883–13

Received May 1995
Revised November 1995

et al.,[4] Jennious and Turner,[5] Copenhaver *et al.*,[6] Hah *et al.*,[7] Shi and Ribando,[8] Bansod and Rhie[9] and Zhang *et al.*[10] In solving the three-dimensional Navier–Stokes (N–S) equations, some researchers, including Casey *et al.*,[1] Copenhaver *et al.*[6] and Hah *et al.*,[7] also predict the operating range of compressor impellers.

Since the operating condition for centrifugal machinery often necessitates the operation of the impeller at off-design points, knowing the flow performance under such conditions is as important as knowing that under the design condition. In this paper, attention is focused on the internal flow field computation inside a backswept centrifugal impeller at two off-design points. The internal flows within an impeller have been measured in detail at five cross-sections by Farge and Johnson.[11] The flow rates at the off-design points are 85 per cent and 113 per cent of that at the design point. In the present paper, coupled with the k–ϵ two-equation turbulence model, the fully three-dimensional N–S equations are solved by using the computer code TDFFCP (three-dimensional flow field computer programme) developed by Zhang.[12] The calculated results are compared with the experimental ones on the five measurement planes.

GOVERNING EQUATIONS

Since the rotational speed of the backswept centrifugal impeller considered is 500 rev min^{-1} and the impeller tip velocity is 23·8 m s^{-1} for both the off-design flow rate cases considered, the flows inside the impeller are assumed reasonably to be incompressible. For incompressible flows the fully three-dimensional Reynolds- averaged N–S equations with the Boussinesq approximation are expressed relative to a rotating co-ordinate system as

$$\frac{\partial}{\partial X_i}(\rho U_i) = 0, \tag{1}$$

$$\frac{\partial}{\partial X_i}(\rho U_j U_i) = -\frac{\partial p}{\partial X_i} + \frac{\partial}{\partial X_i}\left[(\mu + \mu_t)\left(\frac{\partial U_j}{\partial X_i} + \frac{\partial U_i}{\partial X_j}\right)\right] - \tfrac{2}{3}\rho k \delta_{ij} + \rho\omega^2 \vec{r} - 2\rho\vec{\omega} \times \vec{r}, \tag{2}$$

where U_i are the relative velocity components, μ is the molecular viscosity, μ_t is the eddy viscosity, p is the static pressure, r is the local radius, ρ is the density and ω is the angular speed of rotation.

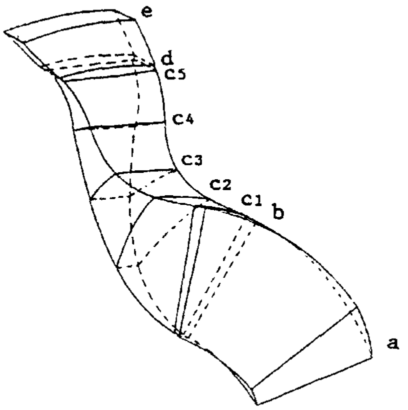

Figure 1. Profile of impeller passage and computational domain: a, flow inlet; b, leading edge; c1–c5, five measurement planes; d, trailing edge; e, flow outlet

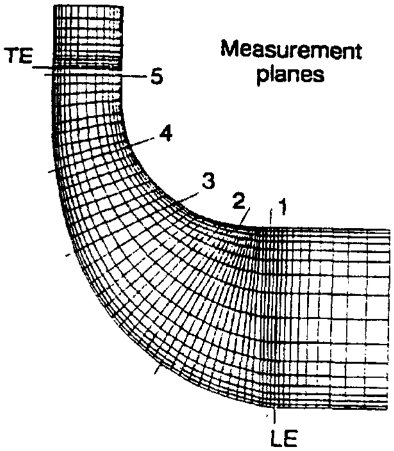

Figure 2. Meridional view of grid and five measurement planes

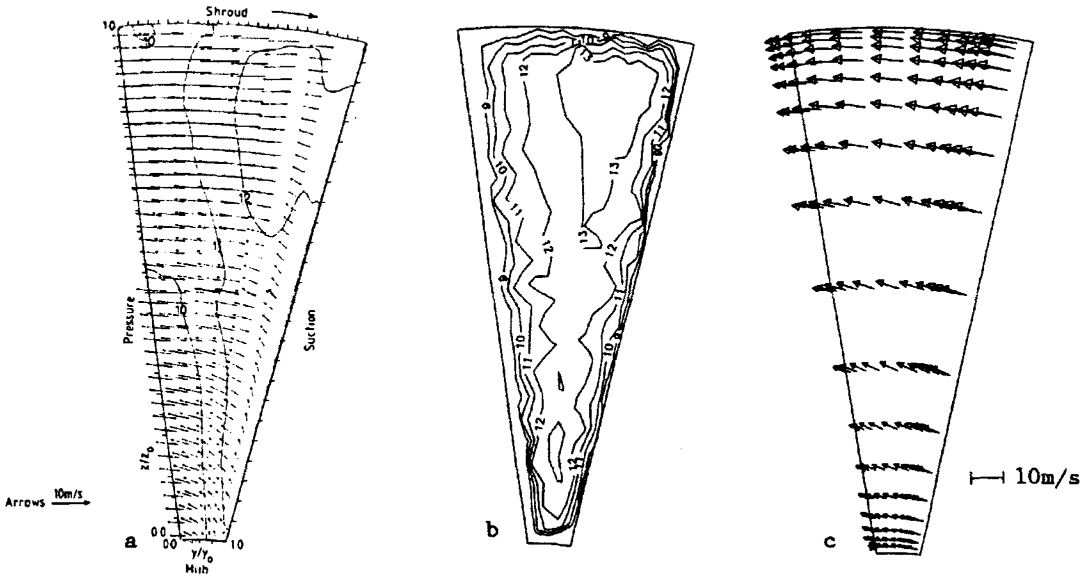

Figure 3. Comparison at plane 1 for above-design flow rate (contours in m s^{-1}): a, velocity measured by Farge and Johnson;[11] b, computed throughflow velocity; c, computed cross-section velocity

In order to close the above equations, i.e. to obtain the eddy viscosity, μ_t, a suitable turbulence model has to be employed. The standard k–ϵ two-equation turbulence model proposed by Launder and Spalding[13] is adopted here:

$$\frac{\partial}{\partial X_i}(\rho U_i k) = \frac{\partial}{\partial X_i}\left(\frac{\mu_t}{\sigma_k}\frac{\partial k}{\partial X_i}\right) + P - \rho\epsilon, \tag{3}$$

$$\frac{\partial}{\partial X_i}(\rho U_i \epsilon) = \frac{\partial}{\partial X_i}\left(\frac{\mu_t}{\sigma_\epsilon}\frac{\partial \epsilon}{\partial X_i}\right) + \frac{\epsilon}{k}(C_1 P - C_2\epsilon), \tag{4}$$

where

$$P = \left[\mu_t\left(\frac{\partial U_i}{\partial X_j} + \frac{\partial U_j}{\partial X_i}\right) - \tfrac{2}{3}\rho k \delta_{ij}\right]\frac{\partial U_j}{\partial X_i}$$

is the rate of production of turbulence kinetic energy and the eddy viscosity μ_t is determined by the relation

$$\mu_t = C_\mu \rho \frac{k^2}{\epsilon}. \tag{5}$$

Here C_1, C_2, σ_k, σ_ϵ and C_μ are empirical constants set to the values

$$C_1 = 1{\cdot}44, \quad C_2 = 1{\cdot}92, \quad C_\mu = 0{\cdot}09, \quad \sigma_k = 1{\cdot}0, \quad \sigma_\epsilon = 1{\cdot}3.$$

The wall function method of Launder and Spalding[13] is used to minimize the number of grid points needed with the laminar sublayer region:

$$U^+ = \frac{1}{K}\ln Y^+ + B. \tag{6}$$

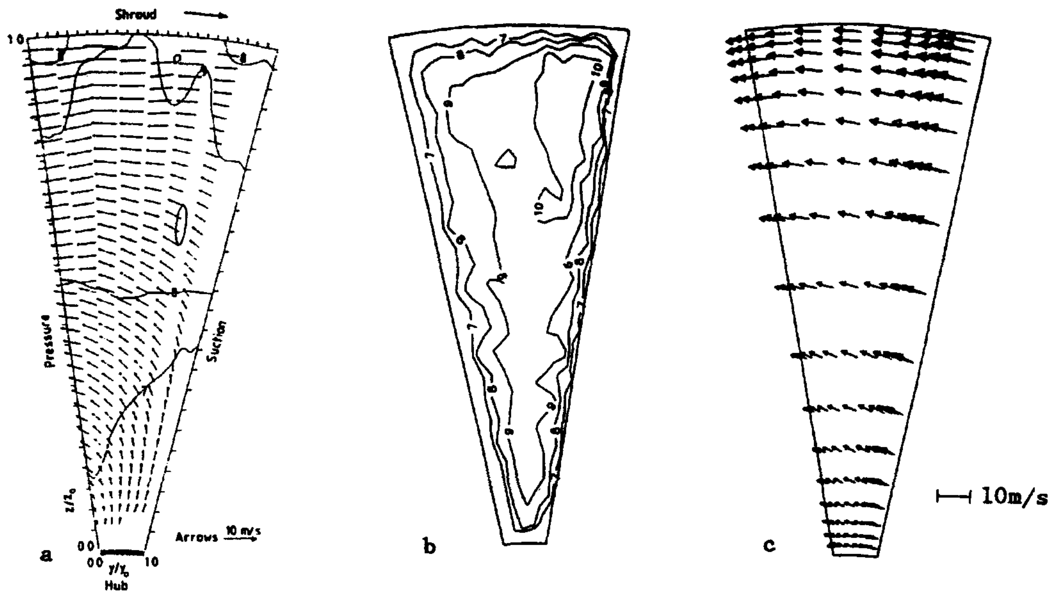

Figure 4. Comparison at plane 1 for below-design flow rate (contours in m s^{-1}): a, velocity measured by Farge and Johnson;[11] b, computed throughflow velocity; c, computed cross-section velocity

The turbulence kinetic energy k and the turbulence kinetic energy dissipation ϵ are obtained as

$$k_\mathrm{p} = \frac{\tau_\mathrm{w}}{\rho C_\mu^{0\cdot5}}, \qquad \epsilon_\mathrm{p} = \frac{C_\mu^{0\cdot75} k_\mathrm{p}^{1\cdot5}}{K Y_\mathrm{p}}. \tag{7}$$

Here K and B are empirical constants set to 0·41 and 5·5 respectively.

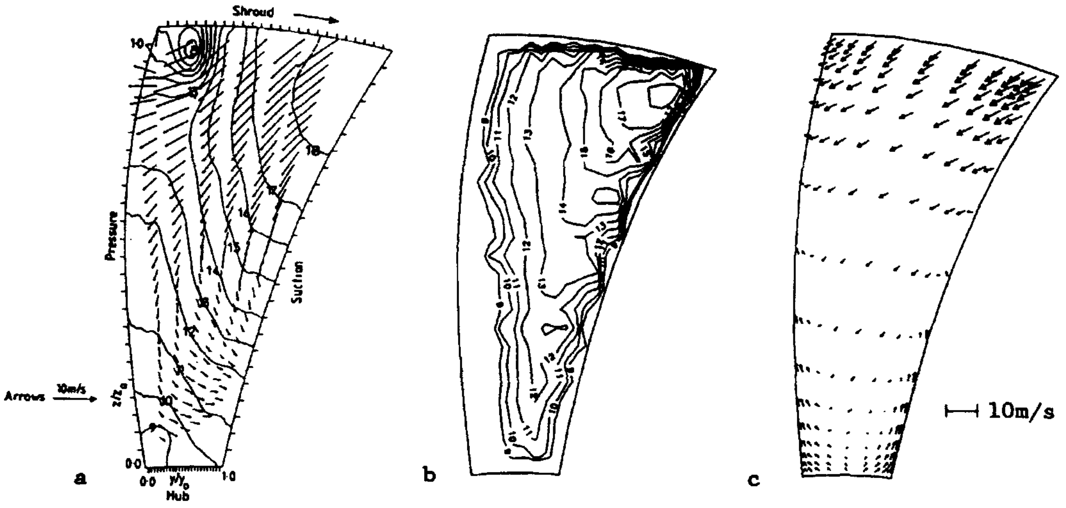

Figure 5. Comparison at plane 2 for above-design flow rate (contours in m s^{-1}): a, velocity measured by Farge and Johnson;[11] b, computed throughflow velocity; c, computed cross-section velocity

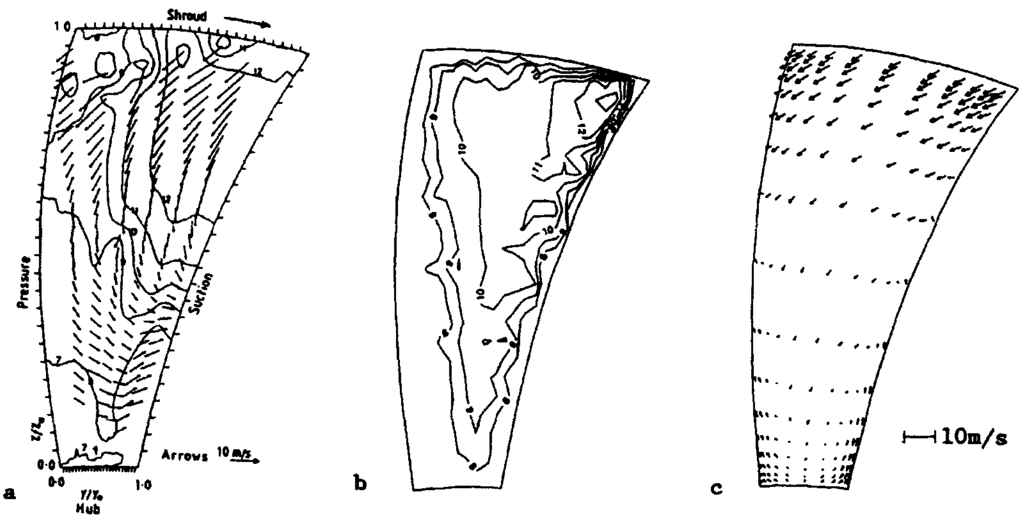

Figure 6. Comparison at plane 2 for below-design flow rate (contours in m s^{-1}): a, velocity measured by Farge and Johnson;[11] b, computed throughflow velocity; c, computed cross-section velocity

NUMERICAL METHODS

Discretized transport equation

The governing equation for an arbitrary dependent variable ϕ can be written in the general form

$$\frac{\partial}{\partial x_i}(\rho U_i \phi) = \frac{\partial}{\partial x_i}\left(\Gamma \frac{\partial \phi}{\partial x_i}\right) + S^{\phi}, \tag{8}$$

where Γ is the effective diffusion coefficient and S^{ϕ} is the source term.

To numerically solve the governing equation for a complex geometry such as that inside a centrifugal impeller, it is convenient to transform it to an arbitrary curvilinear co-ordinate system such as the body-fitted curvilinear co-ordinate system used in the present paper. By using general transformation formulae, the general governing equation (8) can be expressed in the curvilinear co-ordinate sysem (ξ, η, τ) as

$$(\rho G_1 \phi_\xi)_\xi + (\rho G_2 \phi_\eta)_\eta + (\rho G_3 \phi_\tau)_\tau = \left(\frac{\alpha_1}{J}\Gamma \phi_\xi\right)_\xi + \left(\frac{\alpha_2}{J}\Gamma \phi_\eta\right)_\eta + \left(\frac{\alpha_3}{J}\Gamma \phi_\tau\right)_\tau + JS^{\phi} + S, \tag{9}$$

where

$$G_1 = J(\xi_x U + \xi_y V + \xi_z W), \qquad G_2 = J(\eta_x U + \eta_y V + \eta_z W), \qquad G_3 = J(\tau_x U + \tau_y V + \tau_z W),$$

$$\alpha_1 = \xi_x^2 + \xi_y^2 + \xi_z^2, \qquad \alpha_2 = \eta_x^2 + \eta_y^2 + \eta_z^2, \qquad \alpha_3 = \tau_x^2 + \tau_y^2 + \tau_z^2,$$

$$S = (J\Gamma\beta_1\phi_\eta)_\xi + (J\Gamma\beta_1\phi_\xi)_\eta + (J\Gamma\beta_2\phi_\xi)_\eta + (J\Gamma\beta_2\phi_\eta)_\tau + (J\Gamma\beta_3\phi_\xi)_\tau + (J\Gamma\beta_3\phi_\tau)_\xi,$$

$$\beta_1 = \xi_x\eta_x + \xi_y\eta_y + \xi_z\eta_z, \qquad \beta_2 = \eta_x\tau_x + \eta_y\tau_y + \eta_z\tau_z, \qquad \beta_3 = \xi_x\tau_x + \xi_y\tau_y + \xi_z\tau_z$$

and J is the Jacobian matrix.

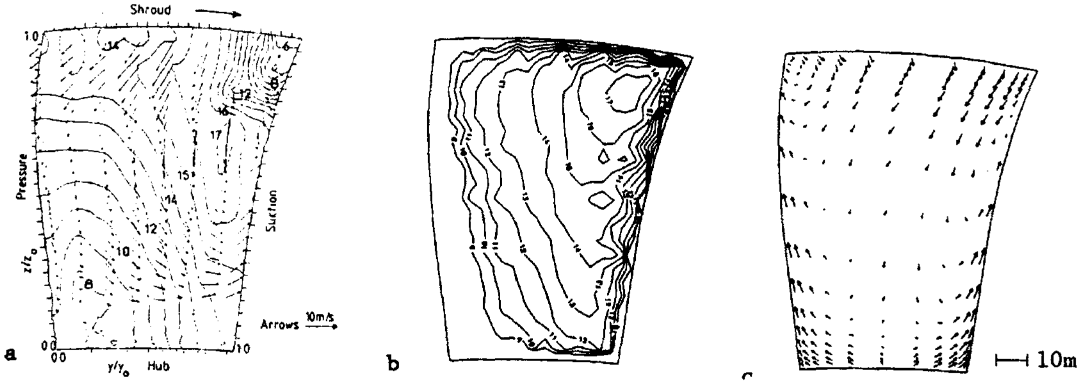

Figure 7. Comparison at plane 3 for above-design flow rate (contours in m s^{-1}): a, velocity measured by Farge and Johnson;[11] b, computed throughflow velocity; c, computed cross-section velocity

Integrated over a control volume, the general governing equation (9) can be made to yield a finite difference expression with the power-law scheme of Patankar:[14]

$$A_P\phi_P = \sum_{i}^{\text{NEWSUD}} A_i\phi_i + (JS^\phi + S)\,\delta\xi\,\delta\eta\,\delta\tau, \tag{10}$$

where subscript P stands for the centre of a control volume and subscripts N, E, W, S, U and D stand for the neighbouring points. A_i is a complicated function consisting of convection, diffusion and area terms. A typical A_E is

$$A_E = D_e A(|PE_e|) + \max(-F_e, 0),$$

where

$$D_e = \frac{(J\Gamma\alpha_1)_e\,\delta\eta\,\delta\tau}{(\delta\xi)_e}, \qquad F_e = (\rho G_1)_e\,\delta\eta\,\delta\tau,$$

$$PE_e = F_e/D_e, \qquad A(|PE|) = \max[0, (1 - 0{\cdot}1|PE|)^5],$$

$$A_P = A_N + A_E + A_W + A_S + A_U + A_D.$$

Subscript 'e' refers to the control volume face, i.e. a point between control volume centres P and E.

Pressure correction equation

The above general governing equation (10) is solved for momentum and turbulent scalar variables; another equation should be used for pressure. Since the velocity fields obtained with the intermediate pressure field may not satisfy mass conservation, the pressure field is adjusted to satisfy the continuity equation:

$$U = U^* + U', \qquad V = V^* + V', \qquad W = W^* + W', \qquad p = p^* + p', \tag{11}$$

where an asterisk denotes an intermediate value and a prime denotes a correction. The correlations between pressure correction and contravariant velocity corrections are obtained as

$$G_1' = B_1P_\xi' + C_1P_\eta' + D_1P_\tau', \tag{12a}$$

$$G_2' = B_2P_\xi' + C_2P_\eta' + D_2P_\tau', \tag{12b}$$

$$G_3' = B_3P_\xi' + C_3P_\eta' + D_3P_\tau', \tag{12c}$$

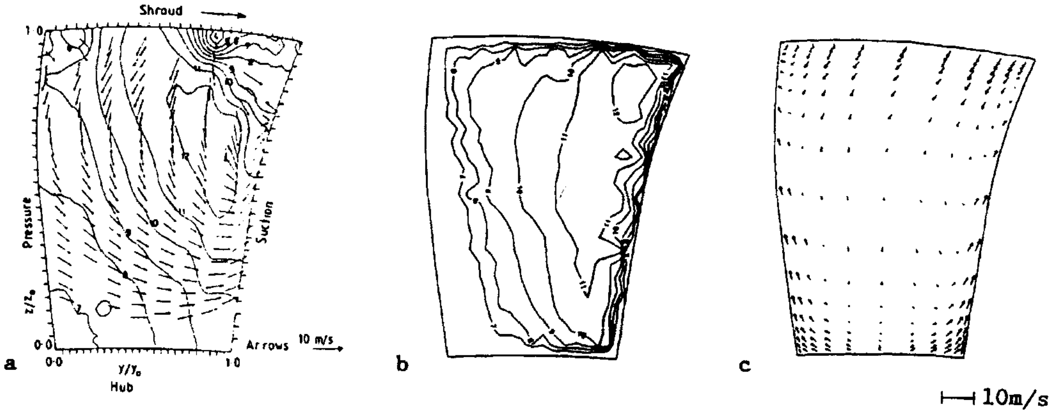

Figure 8. Comparison at plane 3 for below-design flow rate (contours in m s^{-1}): a, velocity measured by Farge and Johnson;[11] b, computed throughflow velocity; c, computed cross-section velocity

where

$$B = -\frac{\xi_x J\ \delta\xi\ \delta\eta\ \delta\tau}{A_\mathrm{P}}, \qquad C = -\frac{\eta_x J\ \delta\xi\ \delta\eta\ \delta\tau}{A_\mathrm{P}}, \qquad D = -\frac{\tau_x J\ \delta\xi\ \delta\eta\ \delta\tau}{A_\mathrm{P}}$$

and the other coefficients have analogous forms.

Based on the continuity equation, the pressure correction equation is expressed as

$$A_\mathrm{P}P'_\mathrm{P} = \sum_{i}^{\mathrm{NEWSUD}} A_i P'_i + S^P \tag{13}$$

where $A_\mathrm{P} = A_\mathrm{N} + A_\mathrm{E} + A_\mathrm{W} + A_\mathrm{S} + A_\mathrm{U} + A_\mathrm{D}$, $A_\mathrm{E} = (\rho B_1)_\mathrm{e}\ \delta\eta\delta\tau/\delta\xi$ (the other coefficients have analogous forms) and $S^P = (\rho G_1\ \delta\eta\ \delta\tau)|_\mathrm{w}^\mathrm{e} + (\rho G_2\ \delta\xi\ \delta\tau)|_\mathrm{s}^\mathrm{n} + (\rho G_3\ \delta\xi\ \delta\eta)||_\mathrm{d}^\mathrm{u} + [(C_1 P'_\eta + D_1 P'_\tau)]|_\mathrm{w}^\mathrm{e} + [(B_2 P'_\xi + D_2 P'_\tau)\ \delta\xi\ \delta\tau]|_\mathrm{s}^\mathrm{n} + [(B_3 P'_\xi + C_3 P'_\eta)\ \delta\xi\ \delta\eta]|_\mathrm{d}^\mathrm{u}$.

Further details are given in Reference 12.

A non-staggered grid arrangement, i.e. all dependent variables are defined at the same grid location, is employed to minimize the computer storage and the number of interpolations of different control volume centres used in a staggered grid arrangement. A special treatment proposed by Rhie and Chow,[15] namely a high-order interpolation scheme used to evaluate mass fluxes, can prevent

Table I. Geometry of backswept centrifugal impeller

Outlet diameter	909·3 mm	Inlet diameter	571·5 mm
Hub diameter	177·8 mm	Axial length	241·3 mm
Outlet width	72·4 mm	Number of blades	19

Table II. Flow rates

	Below-design flow	Design flow	Above-design flow
Passage flow rate (kg s^{-1})	0·1120	0·1318	0·1482

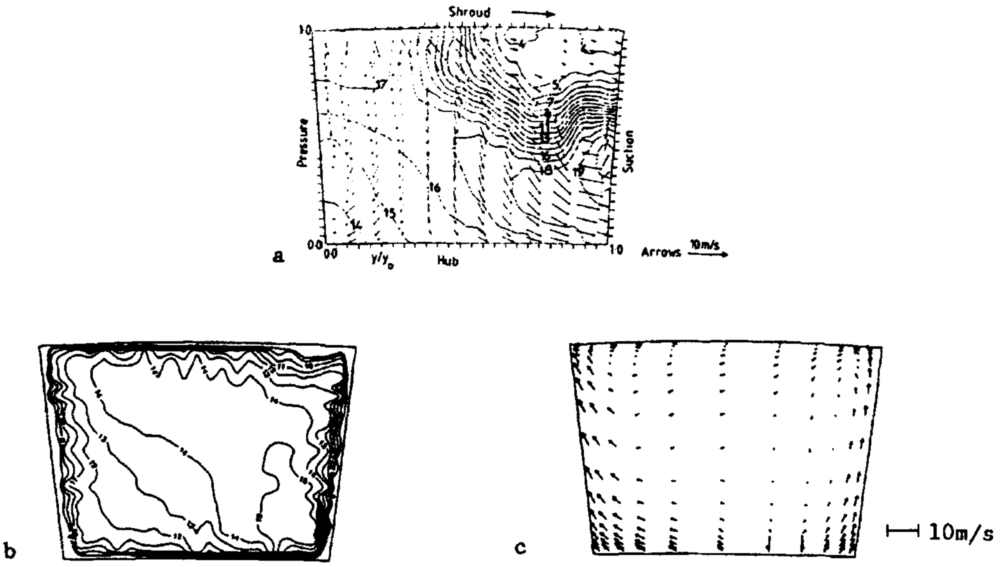

Figure 9. Comparison at plane 4 for above-design flow rate (contours in m s^{-1}): a, velocity measured by Farge and Johnson;[11] b, computed throughflow velocity; c, computed cross-section velocity

pressure oscillations. Since the non-staggered grid arrangement method is easier to implement than the staggered grid arrangement method, especially for a three-dimensional complex geometry, it has gained popularity with researchers such as Bansod and Rhie,[9] Peric,[16] Miller and Schmidt,[17] Lapworth,[18] Acharya and Mooukalled,[19] Coelho *et al.*[20] and Shi and Ribando.[8] In the present computation the non-staggered grid arrangement is employed.

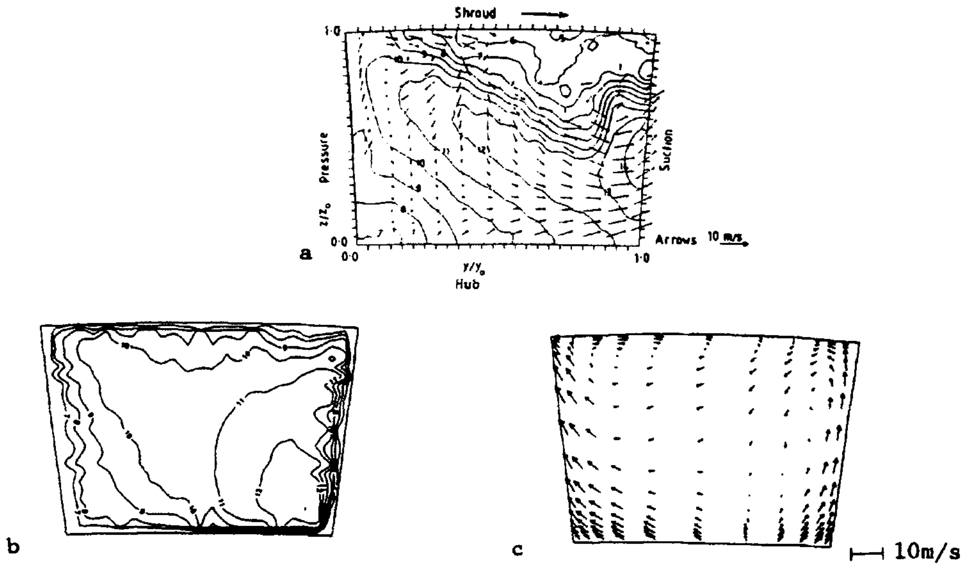

Figure 10. Comparison at plane 4 for below-design flow rate (contours in m s^{-1}): a, velocity measured by Farge and Johnson;[11] b, computed throughflow velocity; c, computed cross-section velocity

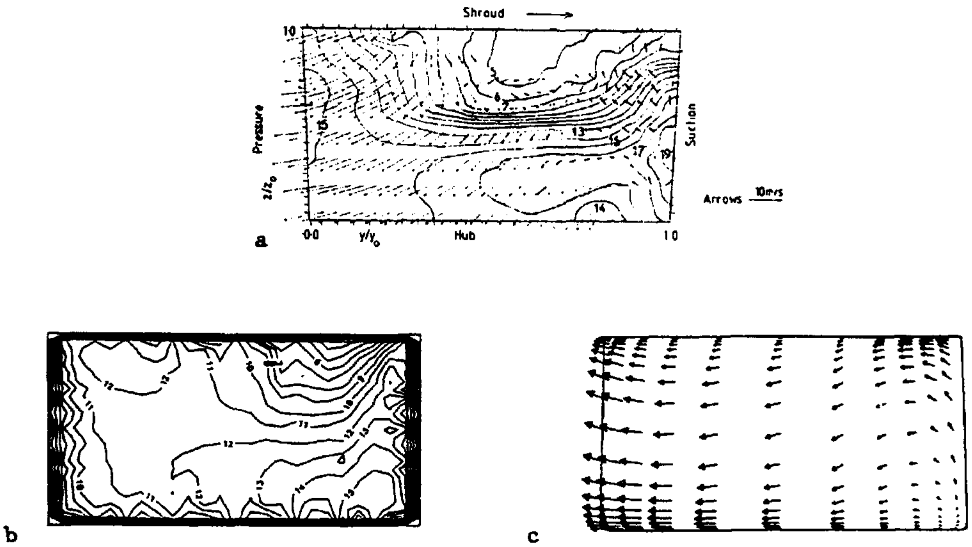

Figure 11. Comparison at plane 5 for above-design flow rate (contours in m s^{-1}): a, velocity measured by Farge and Johnson;[11] b, computed throughflow velocity; c, computed cross-section velocity

Solution procedure

1. With an approximate pressure field obtained by a previous iteration or an initial guess, velocity components U, V and W are obtained by solving the momentum equation (9).
2. Solve the pressure correction equation (13).
3. Correct pressure and velocity components with the pressure correction.
4. Solve the k- and ϵ-equations.
5. Return to step 1 until satisfactory convergence is achieved. In the present computation the maximum ratio of mass residual to inlet mass flow rate is used as the convergence criterion. When the ratio is less than 1×10^{-5}, the computation is assumed to be converged.

Boundary conditions and computational details

The key geometry of the backswept centrifugal impeller is listed in Table I. The detailed geometry can be found in References 11 and 21.

The flow rates at design and off-design points for one impeller passage are given in Table II.

The rotational speeds for design and off-design points are all 500 rev $\min^{-1}$. The profile of the computational domain of the backswept centrifugal impeller and the five measurement planes are shown in Figure 1. The locations of the five measurement planes are given in Reference 21.

The same $13 \times 19 \times 63$ computational grid with 15,561 nodes in total is used for all the calculations at the two off-design flow rates. There are 19 nodes from the hub to the shroud, 13 nodes from the pressure side to the suction side and 63 nodes from the inlet to the outlet of the computational domain. The blade leading edge is at the 11th node and the trailing edge at the 53rd node. A meridional view of the computational grid is shown in Figure 2. Two other grids, $11 \times 15 \times 53$ and $11 \times 15 \times 63$, are also used for computation. Computation results show that most of the flow structure can be captured even with relatively coarse grids.

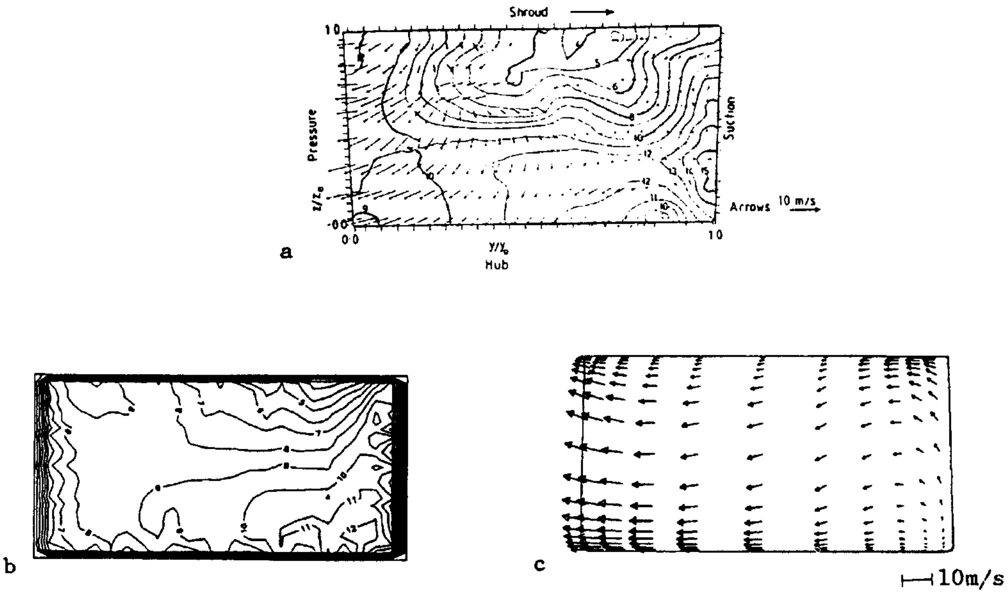

Figure 12. Comparison at plane 5 for below-design flow rate (contours in m s^{-1}): a, velocity measured by Farge and Johnson;[11] b, computed throughflow velocity; c, computed cross-section velocity

Boundary condition treatment is an important part of computation. In the present computation the velocity distribution at the inlet plane of the computational domain has to be specified. Since an extended channel is added before the impeller passage (Figure 1), a uniform inlet velocity distribution can be assumed. The absolute velocity vector in the axial direction is assumed to be uniform and its magnitude is calculated from the specified mass flow rates given in Table II, since there are no measurement data available at this plane. The magnitudes of the absolute velocity vectors in the radial and tangential directions are set to zero. Since the turbulence properties at the inlet plane, turbulence kinetic energy k and turbulence energy dissipation ϵ, are not available from the measurements of Farge and Johnson,[11] the magnitudes of k and ϵ are calculated from widely used empirical relations as

$$k_{\mathrm{in}} = 0{\cdot}05\frac{|\vec{V}|^2}{2}, \tag{14}$$

$$\epsilon_{\mathrm{in}} = \frac{C_\mu k_{\mathrm{in}}^{1\cdot 5}}{0{\cdot}01L}, \tag{15}$$

where $\vec{V}$ is the velocity at the inlet plane and L is the characteristic length. In the present computation L is taken as the hydraulic diameter of the inlet plane.

At the outlet of the computational domain the physical parameters are extrapolated from inner information by setting the values of first-order derivatives along the streamwise direction to be zero for all dependent variables, while the velocity components must satisfy mass continuity.

The relative velocity components at the solid walls are set to zero. Since the wall function of Launder and Spalding[13] is used in the wall regions, the grid lines are condensed to the wall to ensure that the first point is placed in the range $12 \leqslant Y^+ \leqslant 200$.

Besides the inlet, outlet and solid wall conditions, periodic conditions are imposed on the corresponding nodes inside the extended passages before and after the impeller channel, i.e. all parameters are the same on the periodic boundary nodes.

NUMERICAL PREDICTION OF IMPELLER FLOW FIELD

In the measurements of Farge and Johnson[11] a five-hole pressure probe attached to the rotating impeller is used. The resulting signals from the pressure transducers are amplified before passing through slip rings to a microcomputer data acquisition system. Complete details can be found in Reference 21. The measured relative velocities on each of the five measurement planes are presented as the measured velocity components perpendicular to the measurement planes and are depicted by contours, while the remaining components are depicted by arrows. For comparison, the computed velocity components are plotted in the same way. In the present paper the throughflow velocity component refers to that normal to the measurement plane and the cross-section flow refers to that parallel to the measurement plane.

From Figure 3 to Figure 12 the computed results are compared with the measured ones on each of the five measurement planes for both cases, i.e. above the design flow rate and below the design flow rate.

For the throughflow velocity components the measurement shows that the higher- velocity region moves along the suction side from the shroud–suction-side corner to the hub–suction-side corner for each of the two flow rates (all figures denoted ‘a’) and at plane 3 a throughflow velocity defect region (the wake) appears in the shroud–suction-side corner and gradually expands in size towards the exit of the impeller passage (Figures 9–12). At plane 5 the wake occupies a large portion of the flow passage. It seems that the difference in flow rate has little effect on the location and size of the wake.

The present computation successfully predicts a similar throughflow velocity distribution to that illustrated by measurement. The computed velocity magnitudes are close to the measured ones, although there are differences in the initial location of the wake between the computation and measurement. In the computation the wake begins between plane 3 and plane 4 (Figure 9b and 10b)

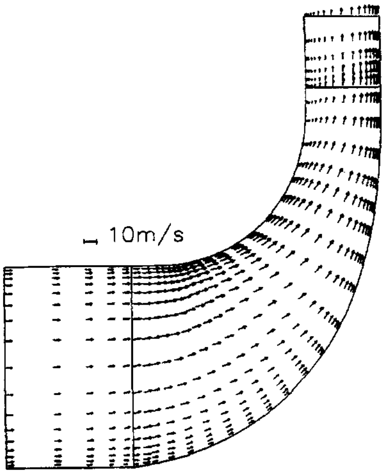

Figure 13. Computed meridional velocity vectors for below-design flow rate (14 per cent pitch section from suction side)

rather than upstream of plane 3 as shown in the measurement (Figures 7a and 8a). At plane 4 the size of the computed wakes is smaller than that of the measured ones (Figures 9a, 9b, 10a and 10b), while at plane 5 the size of the computed wakes is close to that of the measured ones (Figures 11a, 11b, 12a and 12b). The formation of the jet wake structure can be seen more clearly in Figure 13. In the present calculation, even though there is no separation near the shroud for both flow rates, the jet wake structure still occurs.

For cross-section velocity components the measurement at both flow rates shows that from plane 2 to plane 3 an anticlockwise vortex dominates the flow passage, while the computation shows that another clockwise vortex appears near the pressure side. At the other planes the computed cross-section velocity distributions are similar to the measured ones.

CONCLUSIONS

The performance of the backswept centrifugal impeller at off-design points is predicted by solving the three-dimensional N–S equations closed with the k–ϵ two-equation turbulence model. The predicted velocity distributions are compared with the published measured ones and the comparison shows good agreement. The computed location and size of the wake seem to be independent of the flow rate. The jet wake structure still occurs even though there is no separation.

REFERENCES

1. M. V. Casey, P. Dalbert and P. Roth. 'The use of 3D viscous flow calculation in the design and analysis of industrial centrifugal compressors', *ASME J. Turbomach.*, **114**, 27–37 (1992).
2. J. D. Denton, 'The calculation of three-dimensional viscous flow through multistage turbomachines', *ASME J. Turbomach.*, **114**, 18–26 (1992).
3. W. N. Dawes, 'Toward improved throughflow capability: the use of three-dimensional viscous flow solvers in a multistage environment', *ASME J. Turbomach.*, **114**, 8–17 (1992).
4. M. D. Hathaway, J. R. Wood and C. A. Wasserbauer, 'NASA low-speed centrifugal compressor for 3D viscous code assessment and fundamental flow physics research', *ASME Paper 91-GT-140*, 1991.
5. I. K. Jennious and M. G. Turner, 'Three-dimensional Navier–Stokes computations of transonic fan flow using an explicit flow solver and an implicit k–ϵ solver', *ASME J. Turbomach.*, **115**, 261–272 (1993).
6. W. W. Copenhaver, C. Hah and S. L. Puterbaufh, 'Three-dimensional flow phenomena in a transonic high-throughflow, axial-flow compressor stage', *ASME J. Turbomach.*, **115**, 240–272 (1993).
7. C. Hah, A. C. Bryans, Z. Moussa and M. E. Tomsho, 'Application of viscous flow computations for the aerodynamic performance of a backswept impeller at various operation conditions', *ASME J. Turbomach.*, **110**, 303–311 (1988).
8. Q. Shi and R. J. Ribando, 'A parabolic numerical procedure for three- dimensional viscous rotating flows', *Int. j. numer. methods fluids*, **17**, 365–384 (1993).
9. P. Bansord and C. M. Rhie, 'Computation of flow through a centrifugal impeller with tip leakage', *AIAA Paper 90-2021*, 1990.
10. M. J. Zhang, C. G. Gu and Y. M. Miao, 'Numerical study of the internal flow field of a centrifugal impeller', *ASME Paper 94-GT- 357*, 1994.
11. T. Z. Farge and M. K. Johnson, 'Effect of flow rate on loss mechanisms in a backswept centrifugal impeller', *Int. J. Heat Fluid Flow*, **13**, 189–196 (1992).
12. M. J. Zhang, 'A CSIMPLE algorithm for viscous flows and the study of compressible effect by computation and experiment', *Ph.D. Thesis*, Xian Jiaotong University, 1993.
13. B. E. Launder and D. B. Spalding, 'The numerical calculation of turbulence flows', *Comput. Methods Appl. Mech. Eng.*, **3**, 269– 289 (1974).
14. S. V. Patankar, *Numerical Heat Transfer and Fluid Flow*, Hemisphere, New York, 1980.
15. C. M. Rhie and W. L. Chow, 'Numerical study of the turbulent flow past an airfoil with trailing edge separation', *AIAA J.*, **21**, 1525–1532 (1983).
16. M. Peric, 'Analysis of pressure–velocity coupling on nonorthogonal grids', *J. Numer. Heat Transfer B*, **17**, 63–82 (1990).
17. T. F. Miller and F. W. Schmidt, 'Use of a pressure-weighted interpolation method for the solution of the incompressible Navier–Stokes equations on a non-staggered grid systems', *J. of Numer. Heat Transfer*, **14**, 213–223 (1987).

18. B. L. Lapworth, 'Examination of pressure oscillations arising in the computation of cascade flow using a boundary-fitted coordinate system', *Int. j. numer. methods fluids*, **8**, 387–404 (1988).
19. S. Acharya and F. H. Mooukalled, 'Improvement to incompressible flow calculation on a non-staggered curvilinear grid', *J. Numer. Heat Transfer B*, **15**, 131–152 (1989).
20. P. Coelho, J. C. F. Pereira and M. G. Carvalho, 'Calculation of laminar recirculating flows using a local non-staggered grid refinement', *Int. j. numer. methods fluids*, **12**, 535–557 (1991).
21. M. W. Johnson and J. Moore, 'The development of wake flow in a centrifugal impeller', *ASME J. Eng. Power*, **102**, 382–390 (1980).